Advanced Functional Materials

ADVANCED FUNCTIONAL MATERIALS
www.afm-journal.de

RESEARCH ARTICLE

Molecular Engineering-Enabled Self-Adaptive Topological Adsorption Interface: Synergistic Hydrophobic Nanoconfinement and Electrostatic Shielding for Highly Stable Zn Anode

Ling Zhu | Jing Tang | Peng Li | Jinyu Li | Chang Yan | Zihan Zhu | Liya Wang | Huibing He | Yuanqin Zhu | Dongdong Li

Guangxi Key Laboratory of Electrochemical Energy Materials, Guangxi Colleges and Universities Key Laboratory of Applied Chemistry Technology and Resource Development, University Engineering Research Center of Green Chemical New Materials, School of Chemistry and Chemical Engineering, Guangxi University, Nanning, Guangxi, China

Correspondence: Huibing He (huibinghe@gxu.edu.cn) | Yuanqin Zhu (yqzhu@gxu.edu.cn) | Dongdong Li (lidd@gxu.edu.cn)

Received: 23 January 2026 | **Revised:** 6 March 2026 | **Accepted:** 11 March 2026

Keywords: electrolyte additive | nanoconfinement | polyhedral oligomeric silsesquioxane | zinc ion batteries | zinc metal anode

ABSTRACT

The Zn metal anodes suffer from severe side reactions and uncontrolled dendrite growth, limiting their practical application. To stabilize the Zn anode, a novel dynamic self-adaptive dual-ion stabilization mechanism is developed via in-situ self-assembly of multifunctional Oktakis (tetramethylammonium)-T_8-silsesquioxane (TMA-POSS) topological molecular additives. In the electrolyte, TMA-POSS dissociates into tetramethyl quaternary ammonium (TMA^+) cations and polyhedral oligomeric silsesquioxane [$T_8(Si\text{-}O)_8^{8-}$] anions. TMA^+ preferentially adsorbs on the Zn surface, forming an inner self-healing electrostatic shielding layer that ensures uniform Zn nucleation and deposition. Concurrently, $T_8(Si\text{-}O)_8^{8-}$ self-organizes into a hydrophobic nanoconfined buffer layer, which synergistically regulates Zn^{2+}/SO_4^{2-} migration, promotes $[Zn(H_2O)_6]^{2+}$ desolvation, and restricts H_2O penetration, thereby suppressing space charge layer-introduced dendrite growth and side reactions. More notably, this self-assembled dual-ion layer dynamically adapts to interfacial changes without degradation, exhibiting high stability and non-sacrificial nature. Consequently, the Zn anode delivers exceptional reversibility 4700 h, and 99.6% Coulombic efficiency over 2110 cycles. Zn//MnO_2 and Zn//V_2O_5 full cells deliver outstanding capacity retentions of 81.2% (1700 cycles at 1 A g^{-1}) and 80.1% (2500 cycles at 10 A g^{-1}), respectively. This work pioneers a novel multifunctional dual-ion interface based on topological molecular engineering, providing a feasible strategy to advance the practical application of aqueous zinc-ion batteries.

1 | Introduction

Aqueous zinc-ion batteries (AZIBs), employing metallic Zn anodes with high natural abundance, high theoretical volumetric/gravimetric capacities (5855 mAh cm^{-3}, 820 mAh g^{-1}), and a favorable redox potential (−0.76 V vs SHE), have attracted considerable attention as promising candidates for grid-scale energy storage owing to their intrinsic safety, cost-effectiveness (25 USD kWh^{-1}), and eco-sustainability [1–4]. Nevertheless, the practical application of AZIBs is impeded by two persistent challenges: thermodynamically driven side reactions and kinetically uncontrolled Zn dendrite growth.

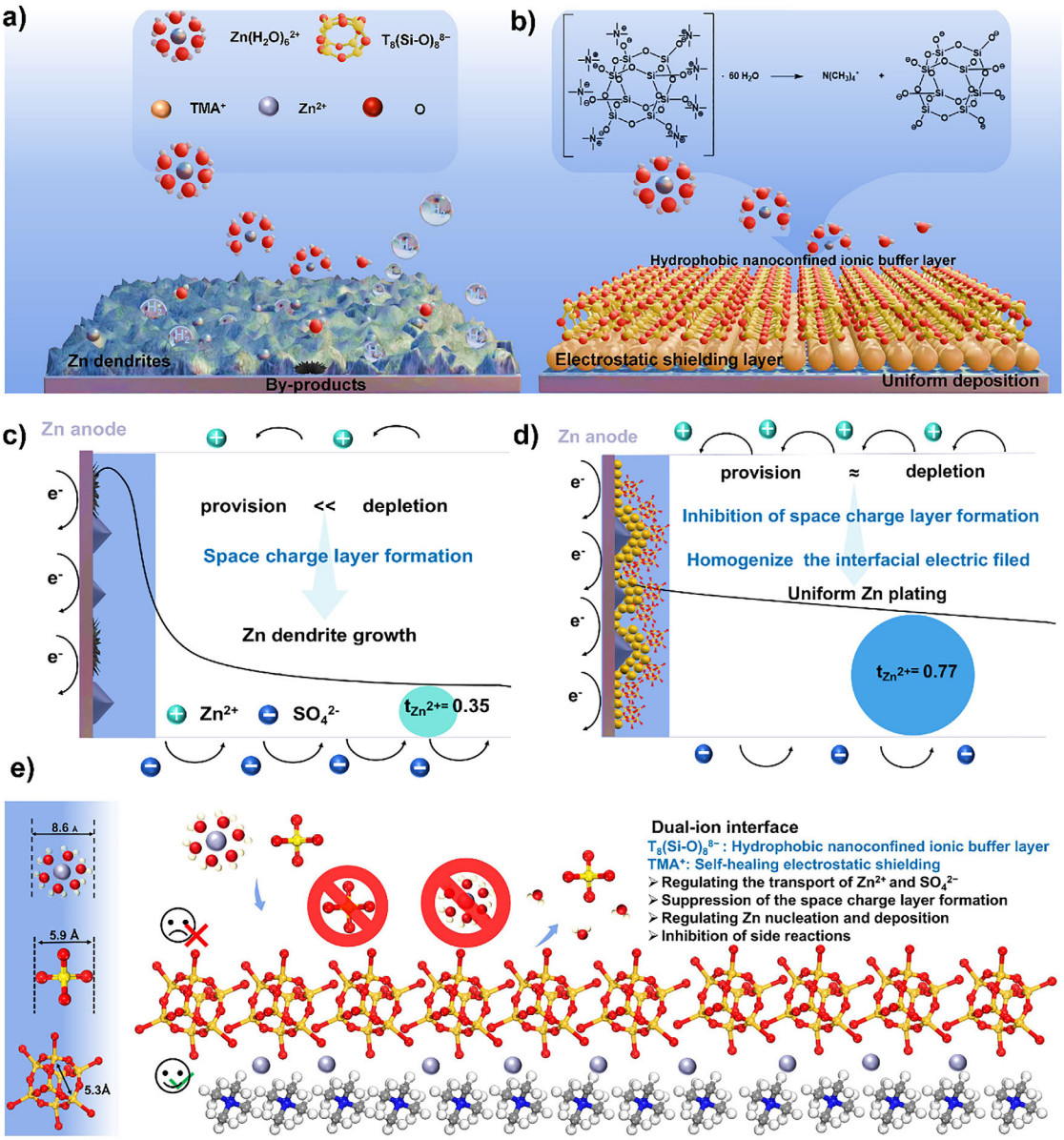

FIGURE 1 | Schematic diagram of the Zn^{2+} deposition at the anode/electrolyte interface. a) ZS electrolyte and b) ZS/TMA-POSS electrolyte. c) The common problems existing in the typical ZS electrolyte and d) solution of tuning kinetics behavior based on the space-charge model. e) Schematic of nanoconfinement of $T_8(Si\text{-}O)_8^{8-}$ anions.

The inherent thermodynamic instability of metallic Zn in near-neutral (weakly acidic) aqueous electrolytes induces preferential H^+ reduction over Zn^{2+} upon exposure to H_2O, triggering spontaneous hydrogen evolution reaction (HER) and corrosion [5, 6]. This process causes gas evolution and interfacial OH^- accumulation, which subsequently drives OH^-/SO_4^{2-} co-precipitation to form $Zn_4SO_4(OH)_6{\cdot}xH_2O$ (ZSH) passivation layers (Figure 1a). These coupling side reactions consume active Zn, increase interfacial impedance, and disrupt Zn^{2+} flux, leading to rapid capacity decay and reduced Coulombic efficiency (CE) [7]. Additionally, $Zn(H_2O)_6^{2+}$ desolvation release reactive H_2O at the Zn anode/electrolyte interface, which not only exacerbates side reactions but also impedes the desolvation kinetics [8]. Thus, designing a hydrophobic interface to minimize H_2O-Zn contact constitutes a critical pathway for suppressing side reactions and improving electrochemical kinetics [9, 10].

]Dendritic growth stems from the self-amplifying interplay between the "tip effect" and space charge layer-intensified heterogeneous Zn deposition, a kinetically controlled process [5, 11, 12]. Fragile dendrites generate "dead Zn," disrupt Zn^{2+} flux and interfacial electric field, and expand the active surface for side reactions, severely impairing Zn anode reversibility [13]. After $Zn(H_2O)_6^{2+}$ desolvation, Zn^{2+} preferentially reduces at surface protrusions with high local electric fields. This spatially selective deposition amplifies local current density and triggers inhomogeneous Zn nucleation, leading to subsequent Zn deposition that preferentially occurs on pre-existing nuclei, thereby exacerbating interfacial field distortion and driving autocatalytic dendritic growth [7]. More critically, according to Chazalviel's model [14, 15], the kinetic imbalance between Zn^{2+} provision and consumption during electrodeposition causes severe interfacial concentration polarization. Concomitant anion depletion creates

a space charge layer near the Zn anode and a quasi-neutral region in the bulk electrolyte [16]. The localized electric field within this space charge layer amplifies interfacial electric field distortion and the "tip effect," significantly accelerating dendrite growth (Figure 1c) [17–19]. Therefore, controlling Zn nucleation and suppressing space charge layer formation are crucial to inhibit dendrite growth.

Anchoring anions or enhancing cation transport to match Zn^{2+} replenishment with fast Zn deposition kinetics represents effective strategies for suppressing space charge layer formation [11]. For instance, Zhi et al. employed β-cyclodextrin as an anion capturer to diminish SO_4^{2-} depletion, thereby suppressing space charge layer-introduced dendrite formation [20]. Pan et al. utilized the steric hindrance effect of reduced glutathione to align Zn^{2+} reduction kinetics with Zn^{2+} migration, achieving dendrite-free Zn deposition [5]. These approaches have substantially enhanced AZIBs performance. However, simultaneously optimizing interfacial ion migration, regulating Zn nucleation and deposition, and maintaining long-term suppression of side reactions remains a major challenge in practical implementation.

To date, strategies including Zn anode surface design [21–23], electrolyte engineering [10, 24–26], and artificial interface layer [16, 27, 28] have been adopted to stabilize the Zn anode. Among these, electrolyte additives are particularly promising due to their high efficiency and operational simplicity [29]. However, during long-term cycling, the interfacial microenvironment of the Zn anode and its volume/surface morphology undergo continuous evolution, causing delamination and failure of the additive-derived interfacial layer [10, 31]. Repeated interfacial layer reconstruction and gradual electrochemical degradation of the additives inevitably reduce their effective concentration, leading to additive failure. Beyond these limitations, many additives are costly or environmentally incompatible [30]. Therefore, developing electrochemically stable, non-sacrificial, and economically feasible multifunctional additives that are capable of enabling adaptive, dynamic protection for the Zn anode is essential to realize sustainable and long-term stable AZIBs [31].

Polyhedral oligomeric silsesquioxane (POSS) represents the smallest class of molecularly precise silica nanoparticles (1–3 nm in diameter), featuring well-defined topologies and distinctive organic-inorganic hybrid characteristics. Its nanocage-like inorganic core, composed of a hydrophobic siloxane-bridged Si−O−Si framework, is typically surface-functionalized with eight reactive organic groups. This unique molecular architecture combined with tunable surface chemistry enables the widespread application of POSS in fabricating advanced materials with tailored structures and properties [32]. Furthermore, the intrinsic self-assembly capability of POSS enables the spontaneous formation of ordered nanostructures [33], making it as a key nano-building block for constructing structurally precise materials [34].

In our previous work, we leveraged the hydrophobic nature of POSS to create a gel protective layer via microphase separation [35]. However, the continuously evolving Zn anode interface during cycling impacts the stability of this pre-formed layer. In contrast, the electrolyte additive strategy offers simpler processing and better compatibility. Herein, we report a non-sacrificial, low-cost, and multifunctional Oktakis (tetramethylammonium)-T_8-silsesquioxane (TMA-POSS) additive that undergoes in situ self-assembly to form a topologically ordered dual-ion structure at the Zn anode/electrolyte interface (Figure 1b). Enabled by a novel dynamic self-adaptive dual-ion stabilization mechanism, this innovative additive achieves long-term Zn anode stability.

Conventional POSS materials are typically highly hydrophobic, however, TMA-POSS is functionalized with eight tetramethyl quaternary ammonium (TMA^+) cations on its nanocage-like Si–O–Si framework, enabling it to undergo self-ionization in aqueous solution and release positively charged TMA^+ cations along with negatively charged polyhedral oligomeric silsesquioxane [$T_8(Si\text{-}O)_8^{8-}$] anion (Figure S1). These charged species engage in strong ion-dipole interactions with polar H_2O, thereby imparting aqueous solubility to the hydrophobic Si–O–Si nanocage. Our investigations reveal a self-adaptive dual-ion stabilization mechanism: The TMA^+ cations form an inner self-healing electrostatic shielding layer [36] that homogenizes Zn nucleation and guides dense Zn deposition; Meanwhile, the $T_8(Si\text{-}O)_8^{8-}$ anions self-assemble into a hydrophobic nanoconfined ionic buffer layer above the TMA^+ layer, dynamically optimizing interfacial distribution of Zn^{2+} and SO_4^{2-} while inhibiting space charge layer-introduced Zn dendrite growth and suppressing H_2O-introduced side reactions (Figure 1d,e). Unlike conventional additives that form sacrificial interfacial layers via decomposition, neither TMA^+ nor $T_8(Si\text{-}O)_8^{8-}$ participates in interfacial electrochemical reactions, demonstrating an intrinsic non-sacrificial nature. More impressively, this dynamic dual-ion structure exhibits superior interfacial adaptability compared to conventional static SEI or interfacial protective layers. The Zn anode achieves exceptional cycling stability exceeding 4700 h at 1 mA cm^{-2}, 0.5 mAh cm^{-2}. Even under harsh conditions of 10 mA cm^{-2}, 5 mAh cm^{-2} and a high depth of discharge (DOD) of 51.35%, it still demonstrates extended durability of 850 h and 500 h, respectively. The Zn//Cu asymmetric cell retains a high Coulombic efficiency (CE) of 99.6% over 2110 cycles at 1 mA cm^{-2}, 0.5 mAh cm^{-2}. Furthermore, Zn//MnO_2 and Zn//V_2O_5 full cells deliver outstanding capacity retentions of 81.2% (after 1700 cycles, 1 A g^{-1}) and 80.1% (after 2500 cycles, 10 A g^{-1}), respectively. This work establishes a novel dynamic interfacial regulation mechanism through an efficient, cost-effective strategy, providing valuable insights for interfacial engineering design for other metal anode systems.

2 | Results and Discussion

2.1 | Impact of TMA-POSS on Zn^{2+} Solvation Behavior

As depicted in Figure 1e, the $T_8(Si\text{-}O)_8^{8-}$ anion features a well-defined topological molecular structure characterized by a nanocage-like Si−O−Si framework with a precisely defined pore diameter of 4.5 Å [35]. These pores are large than Zn^{2+} (1.5 Å) but smaller than both $[Zn(H_2O)_6]^{2+}$ (8.6 Å) and SO_4^{2-} (5.9 Å) [37] (Figure 1e), enabling steric hindrance against the migration of $[Zn(H_2O)_6]^{2+}$ and SO_4^{2-} while promoting $[Zn(H_2O)_6]^{2+}$ desolvation, thus endowing the $T_8(Si\text{-}O)_8^{8-}$ with a distinctive nanoconfinement effect. Simultaneously, the high electronegativity of the $T_8(Si\text{-}O)_8^{8-}$ anion enables the $T_8(Si\text{-}O)_8^{8-}$ layer to strongly constrain SO_4^{2-} migration while enhance Zn^{2+} transport via electrostatic interaction, thereby mitigating space charge

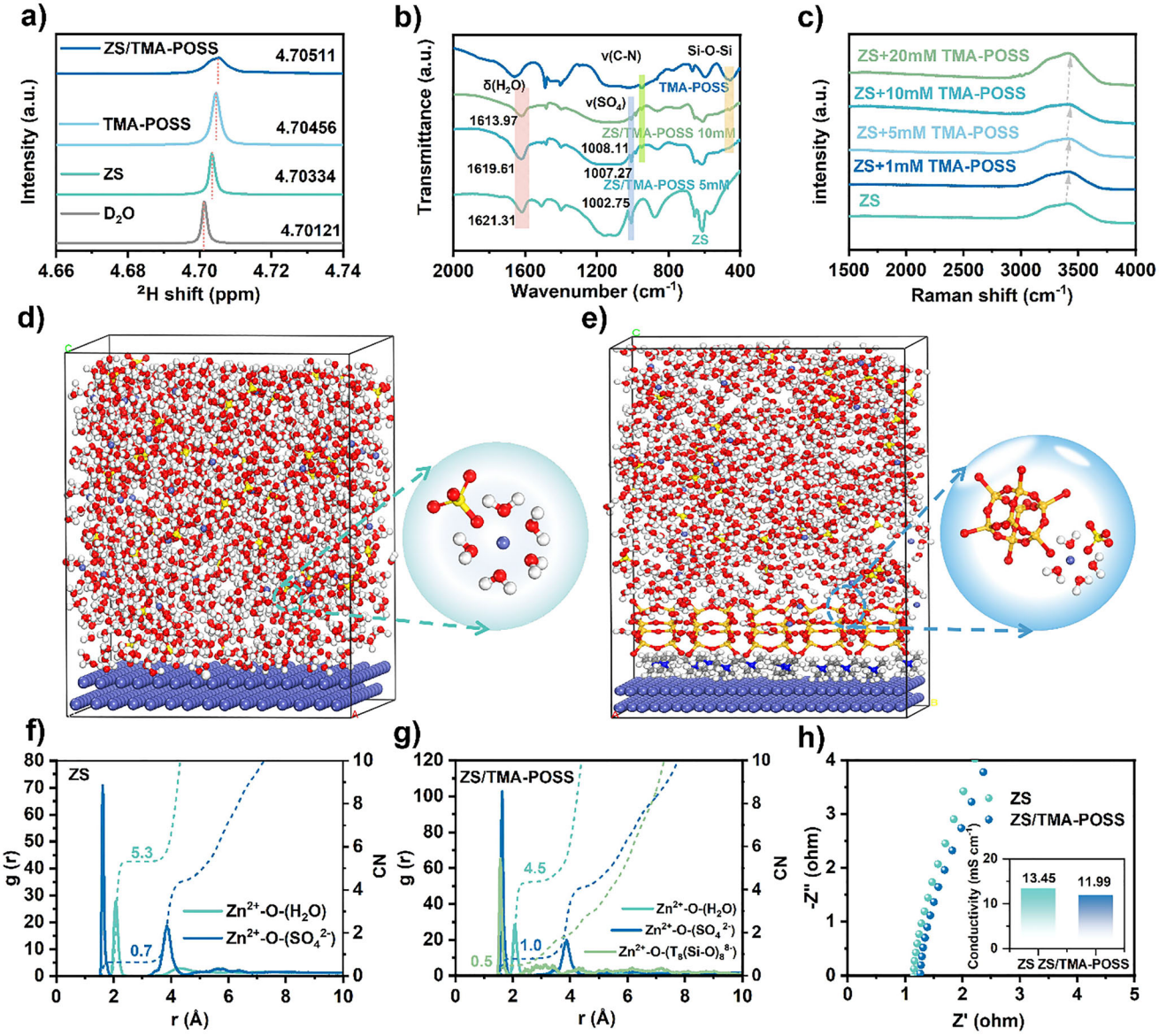

FIGURE 2 | Evolution of the Zn^{2+} solvation structure. a) ^2H NMR spectra of different solutions. b) FTIR spectra. c) Raman spectra of O–H stretching band. MD simulation snapshots of d) ZS and e) ZS/TMA-POSS electrolytes. RDFs and CNs of Zn^{2+}–O in f) ZS and g) ZS/TMA-POSS electrolytes. h) Ionic conductivity of different electrolytes.

layer formation and modulating Zn deposition behavior. Furthermore, the inherent hydrophobicity of the Si–O–Si framework prevents interfacial H_2O accumulation, effectively suppressing H_2O-induced side reactions.

^2H nuclear magnetic resonance (^2H NMR) measurements were first conducted to investigate the effect of TMA-POSS on $[Zn(H_2O)_6]^{2+}$ desolvation. As shown in Figure 2a, pure D_2O exhibits a ^2H chemical shift at 4.70 ppm. The individual addition of either $ZnSO_4$ or TMA-POSS shifts the ^2H signal to higher fields, suggesting decreased electron density around ^2H due to coordination interactions. Notably, TMA-POSS induces a more pronounced chemical shift than $ZnSO_4$, indicating stronger TMA^+-D_2O coordination than Zn^{2+}-D_2O, thereby reducing the content of free H_2O in the bulk electrolyte. Concurrent addition of $ZnSO_4$ and TMA-POSS results in a broadened peak shifted to a lower field, indicating the incorporation of TMA-POSS into the primary Zn^{2+} solvation shell and partial release of previously coordinated H_2O molecules [18]. With increasing TMA-POSS concentration, the O–H bending vibration at 1621 cm^{-1} in the Fourier transform infrared (FTIR) spectra shows a redshift (Figure 2b), implying weakened hydrogen-bonding interactions among H_2O molecules. Complementary Raman spectra (Figure 2c) exhibit a blue-shifted O–H stretching band in the 3200–3600 cm^{-1} region, indicating reduced H_2O activity [38]. Additionally, the SO_4^{2-} peak in the FTIR spectra exhibits a blue shift (Figure 2b), and the symmetric stretching vibration of SO_4^{2-} at 980 cm^{-1} in the Raman spectra also displays a pronounced blue shift (Figure S2). These spectroscopic signatures are attributed to the electrostatic interaction between SO_4^{2-} and the $T_8(Si\text{-}O)_8^{8-}$ [39], which effectively immobilizes SO_4^{2-} in the electrolyte.

Molecular dynamics (MD) simulations were further employed to investigate the impact of TMA-POSS on the Zn^{2+} solvation

structure. In the blank 2 M $ZnSO_4$ (ZS) electrolyte, Zn^{2+} exists in a coordination state with H_2O and SO_4^{2-}, forming a typical solvation structure (Figure 2d) [40–42]. MD snapshots and Radial distribution functions (RDFs) confirm that TMA-POSS induces rearrangement of the Zn^{2+} solvation shell (Figure 2e). The coordination numbers (CNs) for Zn^{2+}–O (H_2O) and Zn^{2+}–O (SO_4^{2-}) in ZS electrolyte are 5.3 and 0.7, respectively (Figure 2f). However, in the ZS/TMA-POSS electrolyte, the CNs for Zn^{2+}–O (H_2O), Zn^{2+}–O (SO_4^{2-}) and Zn^{2+}–O [$T_8(Si\text{-}O)_8^{8-}$] shift to 4.5, 1.0 and 0.5, respectively (Figure 2g). This structural rearrangement indicates that the $T_8(Si\text{-}O)_8^{8-}$ is incorporated into the Zn^{2+} solvation shell by partially displacing H_2O, thereby facilitating the desolvation of hydrated Zn^{2+} and suppressing interfacial H_2O-induced side reactions.

The unique topological structure of $T_8(Si\text{-}O)_8^{8-}$ imparts a distinctive nanoconfinement effect, and the pronounced electronegativity of the $T_8(Si\text{-}O)_8^{8-}$ anion enables effective suppression of SO_4^{2-} migration and enhanced Zn^{2+} transport through electrostatic interactions. Consequently, the self-assembled dynamic $T_8(Si\text{-}O)_8^{8-}$ layer significantly inhibits space charge layer formation by restricting SO_4^{2-} migration while ensuring sufficient Zn^{2+} provision. As a result of these effects, the addition of TMA-POSS leads to a slight reduction in ionic conductivity (Figure 2h). Nevertheless, Mean square displacement (MSD) calculations (Figure S3) demonstrate an increased Zn^{2+} diffusion coefficient (from 0.01066 to 0.01264 $Å^2\ ps^{-1}$), confirming that TMA-POSS promotes Zn^{2+} transport while simultaneously suppressing SO_4^{2-} migration.

2.2 | Adsorption Behavior of TMA-POSS and Its Impact on Zn Anode Interface

The electrostatic potential (ESP) distributions in Figure 3a and Figure S4 reveal that the entire $T_8(Si\text{-}O)_8^{8-}$ anion exhibits pronounced electronegativity, with the electrostatic potential at its eight oxygen negative centers (−2.29 eV) substantially lower than that of oxygen in H_2O (−1.86 eV). This indicates strong electrostatic repulsion between SO_4^{2-} and $T_8(Si\text{-}O)_8^{8-}$, as well as preferential coordination of Zn^{2+} with $T_8(Si\text{-}O)_8^{8-}$ over Zn^{2+} with H_2O [43]. Density functional theory (DFT) calculations quantitatively validate this trend: as shown in Figure 3b, the adsorption energy (E_{ad}) between $T_8(Si\text{-}O)_8^{8-}$ and Zn^{2+} reaches −3.34 eV, significantly more negative than that of H_2O–Zn^{2+} (−0.23 eV), confirming the $T_8(Si\text{-}O)_8^{8-}$ anion's superior coordination affinity for Zn^{2+} and its ability to replace H_2O from the Zn^{2+} solvation sheath. Notably, The E_{ad} of TMA^+ with Zn (−0.98 eV) exceeds that of H_2O with Zn (−0.31 eV), demonstrating preferential adsorption of TMA^+ on the Zn surface to form an electrostatic shielding layer. Consistent with this interfacial TMA^+ adsorption, the electric double layer capacitance (EDLC) decreases markedly (Figure S5), verifying that adsorbed TMA^+ passivates high-activity tip sites (induced by the "tip effect") and redirects Zn deposition toward homogeneous regions via an electrostatic shielding effect, thereby promoting uniform Zn nucleation and suppressing dendrite growth [44].

Figure 3c and Figures S6 and S7 reveal that the E_{ad} of TMA^+ on the Zn (002), (100), and (101) crystal planes are −1.35, −1.62, and −0.98 eV, respectively. These values are significantly more negative than those of H_2O on the corresponding Zn crystal planes (−0.25, −0.62, and −0.31 eV), further indicating the strong thermodynamic preference of TMA^+ cations for adsorption on the Zn surface. This preferential adsorption displaces H_2O from the Zn anode surface, thereby suppressing side reactions. In contrast, the E_{ad} values of $T_8(Si\text{-}O)_8^{8-}$ on the Zn (002), (100), and (101) crystal planes are only −0.21, −0.15, and −0.17 eV, respectively (Figure S8), which are lower than those of H_2O (−0.25, −0.62, and −0.31 eV) (Figure 3c and Figure S6), Zn^{2+} (−0.22, −0.58, and −0.37 eV) (Figure S9), and TMA^+ (−1.35, −1.62, and −0.98 eV) (Figure 3c and Figure S7) on the same crystal planes, demonstrating that $T_8(Si\text{-}O)_8^{8-}$ does not favor direct adsorption onto the Zn anode surface. Remarkably, upon pre-adsorption of TMA^+, the E_{ad} between $T_8(Si\text{-}O)_8^{8-}$ and Zn (002), (100), and (101) crystal planes increases sharply to −4.83, −4.67, and −5.17 eV, respectively (Figure 3e), indicating spontaneous dual-ion self-assembly of $T_8(Si\text{-}O)_8^{8-}$ atop the TMA^+ layer. This self-organized interfacial architecture is also confirmed by MD simulations, which reveal a well-ordered $TMA^+/T_8(Si\text{-}O)_8^{8-}$ adsorption configuration on the Zn anode surface in 3D snapshots (Figure 2e). Additionally, TMA-POSS reduces the contact angle from 95° to 79° (Figure 3d), further confirming its enhanced zincophilicity and strong interfacial adsorption capability [45].

COMSOL Multiphysics simulations were employed to deeply investigate the effect of TMA-POSS on the dynamic interfacial electric field and Zn^{2+} concentration field distributions. In the ZS electrolyte, the electric field at the tip region becomes increasingly distorted and intensified as Zn deposition proceeds, promoting preferential Zn^{2+} nucleation at these active tips and leading to irregular Zn protrusions and non-uniform Zn^{2+} distribution (Figure 3f,h) [46]. In sharp contrast, the introduction of TMA-POSS achieves uniform electric field and Zn^{2+} distribution (Figure 3g,i) through dual-ion interfacial modulation: (1) The dynamically formed TMA^+ layer exerts an electrostatic shielding effect that redirects Zn^{2+} flux deviate spatially from protrusion tips, guiding Zn deposition toward adjacent flat regions rather than the tip with the minimized surface energy. This suppresses tip-enhanced Zn deposition and homogenizing both the electric field and Zn^{2+} concentration distribution [47, 48]; (2) The $T_8(Si\text{-}O)_8^{8-}$ layer not only significantly homogenizes Zn^{2+} flux and buffers Zn^{2+} transport but also restricts SO_4^{2-} migration via a combination of nanoconfinement effects and electrostatic interactions, thereby effectively suppressing interfacial concentration polarization and enabling dendrite-free Zn deposition.

X-ray photoelectron spectroscopy (XPS) characterizes the adsorption of TMA-POSS on the Zn anode surface. After immersion of Zn foil in ZS/TMA-POSS electrolyte, the XPS spectrum (Figure 4a and Figure S10) reveals a distinct N 1s peak at 400.8 eV, confirming the adsorption of TMA^+. Simultaneously, the detection of Si in the survey spectrum coupled with the Si–O–Si signal at 102.4 eV in the high-resolution Si 2p spectrum (Figure 4b) verifies the adsorption of $T_8(Si\text{-}O)_8^{8-}$. Furthermore, the high-resolution Zn 2p spectrum (Figure S11a) exhibits a noticeable shift in binding energy compared to that obtained from the ZS electrolyte, demonstrating significant changes in the surface coordination environment of Zn [49]. Additional evidence includes a binding energy shift of O 1s and a notable reduction of C–O signal at 286.2 eV (Figure S11b–d), further confirming the successful adsorption of TMA-POSS on the Zn foil surface.

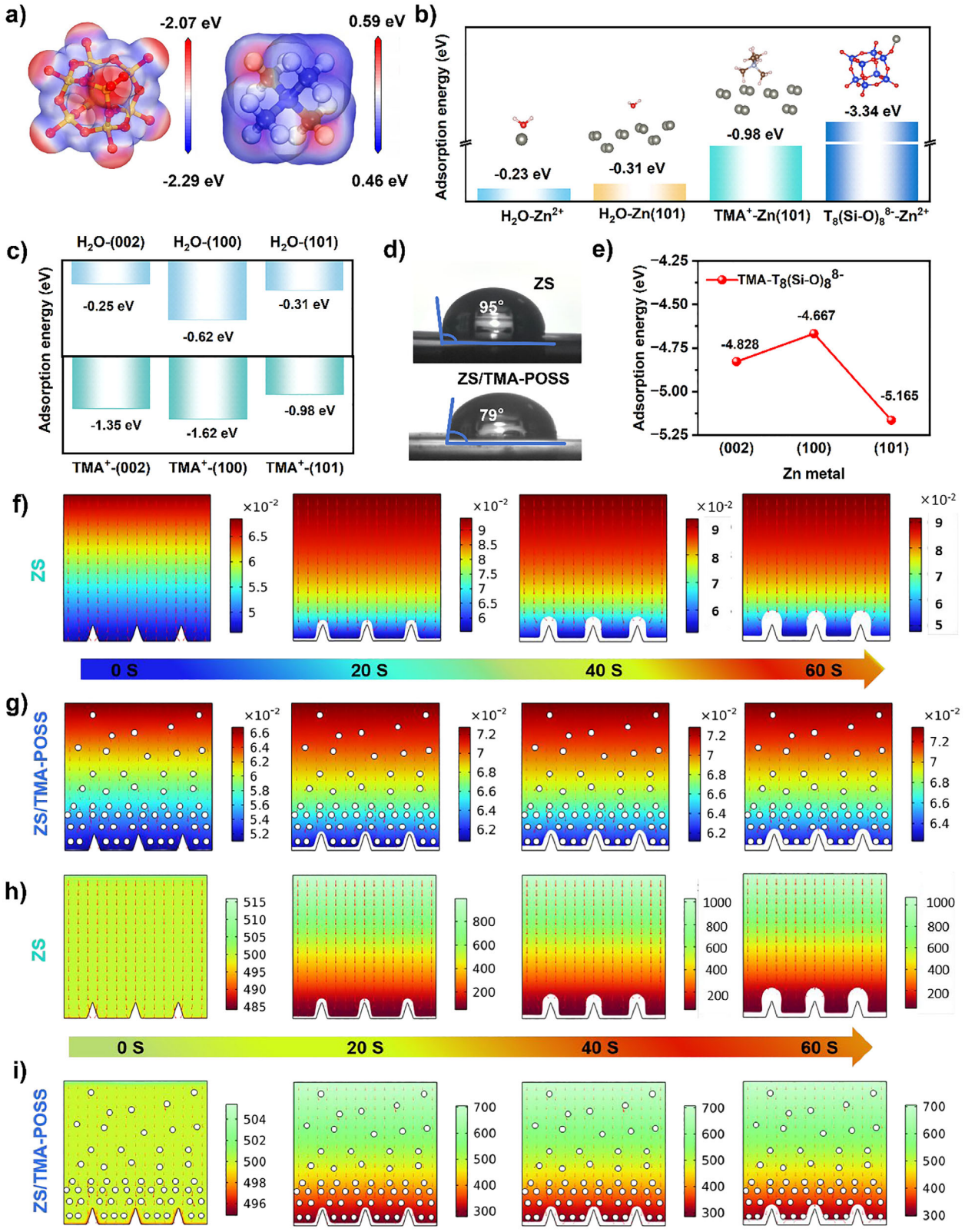

FIGURE 3 | a) ESP mapping of the $T_8(Si\text{-}O)_8^{8-}$ anion and TMA^+ molecule. b) Adsorption energy between Zn with TMA^+ and H_2O molecules, Zn^{2+} ion with $T_8(Si\text{-}O)_8^{8-}$ and H_2O molecules. c) Adsorption energies of TMA^+ and H_2O on the Zn (002), (101) and (100) crystal planes. d) Contact angles of Zn foil with ZS and ZS/TMA-POSS electrolyte. e) $T_8(Si\text{-}O)_8^{8-}$ adsorption energy on different Zn crystal planes after TMA^+ adsorption. The dynamic electric field distribution in f) ZS and g) ZS/TMA-POSS electrolyte. Simulated Zn^{2+} concentration field distribution in h) ZS and i) ZS/TMA-POSS electrolyte.

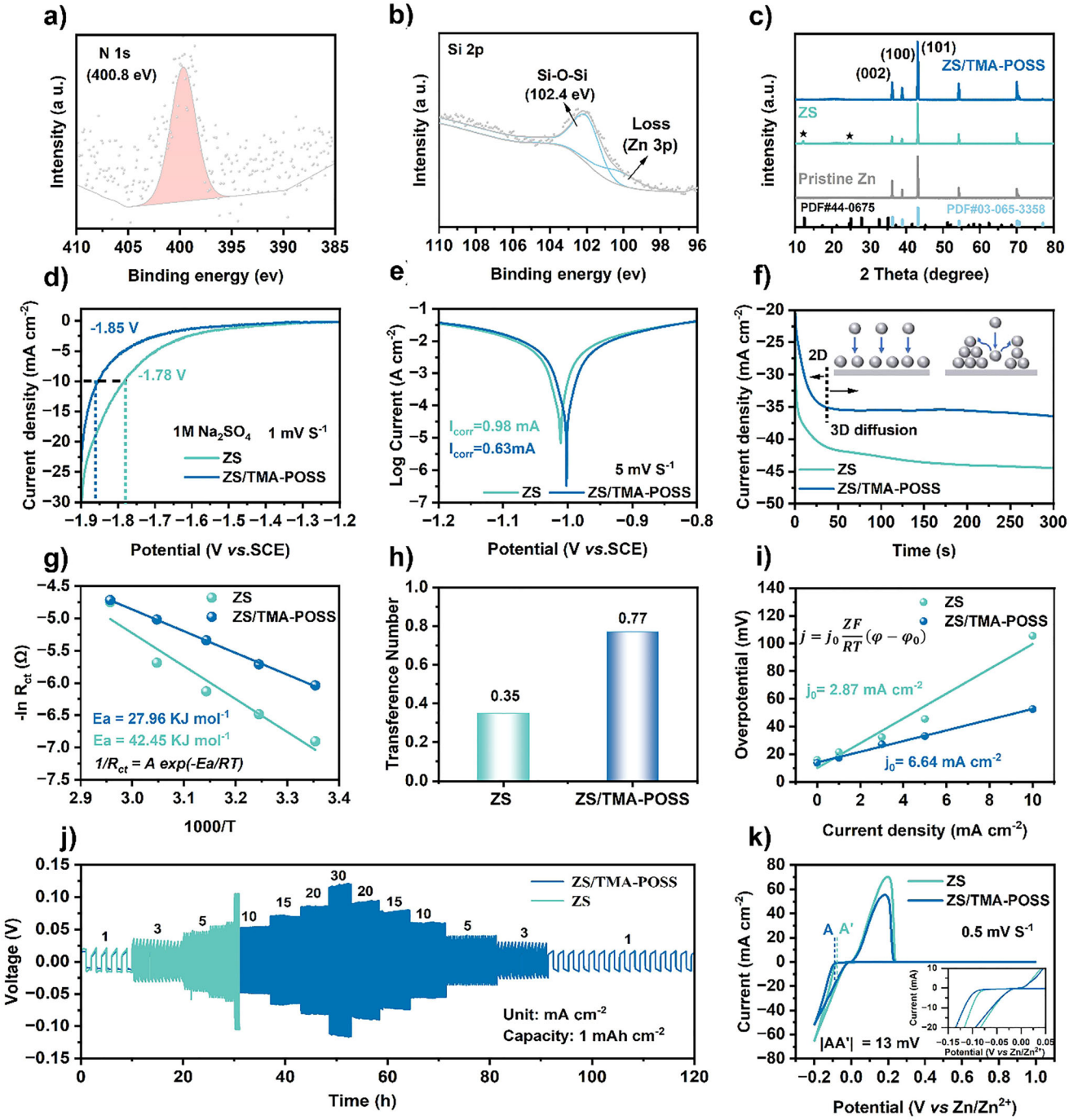

FIGURE 4 | High-resolution a) N 1s and b) Si 2p XPS spectra of the Zn anode after soaking in ZS/TMA-POSS electrolyte for a week. c) XRD patterns of Zn electrodes after 50 cycles at 1 mA cm^{-2}. d) LSV curves profiles acquired in a three-electrode system with a scan rate of 1 mV s^{-1}. e) Tafel curves. f) CA curves of Zn//Zn symmetric cell at a constant overpotential of –150 mV. g) Activation energy of Zn^{2+} desolvation. h) Transference number of Zn^{2+}. i) Exchange current density at various current densities. j) Rate performance of Zn//Zn symmetric cell. k) CV curves of Zn//Cu asymmetric cell.

2.3 | Impact on Zn Anode Stability and Electrochemical Performance

To investigate the suppression of side reactions, Zn foil was immersed in different electrolytes for 7 days and characterized for surface morphology and composition. Compared to the ZS electrolyte, the Zn foil treated with ZS/TMA-POSS retains its pristine bright metallic luster without macroscopic morphological changes (Figure S12a). The scanning electron microscopy (SEM) image shows a smooth and impurity-free surface (Figure S12d). Energy dispersive X-ray spectroscopy (EDS) demonstrates a uniform distribution of C, N, O, Si, and Zn (Figure S13). Crucially, X-ray diffraction (XRD) pattern reveals no detectable peaks of $Zn_4SO_4(OH)_6{\cdot}xH_2O$ (ZHS, PDF#44-0675) by-products (Figure S12b) [50]. These results collectively demonstrate that TMA-POSS adsorbs uniformly on the Zn foil, effectively inhibiting

side reactions. Further XRD analysis after cycling (Figure 4c) also confirms the absence of ZHS, highlighting enhanced interfacial stability and effective suppression of side reactions. The protection mechanism arises from the spontaneous formation of a bilayer structure by $T_8(Si\text{-}O)_8^{8-}$ and TMA^+ on the Zn surface, in which the zincophilic and hydrophobic Si−O−Si nanocage effectively blocks H_2O penetration and thus suppresses H_2O-induced side reactions. Meanwhile, TMA-POSS-mediated Zn deposition exhibits a pronounced preferential orientation of the (101) crystal plane. This deposition behavior effectively suppresses dendrite growth and facilitates uniform Zn deposition [51, 52, 36], highlighting the multifunctionality of TMA-POSS.

The Zn deposition process is inherently coupled with the competing hydrogen evolution reaction (HER), resulting in gas evolution, electrolyte consumption, and an increase in interfacial pH. ZHS formation occurs when the interfacial pH exceeds 5.47 [53], generating insulating deposits that impede ion and electron transport [54]. Given the strong correlation between HER and Zn corrosion kinetics in acidic media, suppression of HER can enhance the corrosion resistance of the Zn anode [8]. The hydrophobic $T_8(Si\text{-}O)_8^{8-}$ nanocage functions as a physical barrier, effectively blocking H_2O access to the Zn surface and thereby significantly inhibiting HER as well as associated corrosion and passivation side reactions. Linear sweep voltammetry (LSV) confirms these effects through a significant increase in the hydrogen evolution overpotential from −1.783 to −1.854 V (Figure 4d). The Tafel curve (Figure 4e) further shows improved corrosion resistance through a reduction in corrosion current density (I_{corr}) from 0.983 to 0.631 mA cm^{-2} and a more favorable corrosion potential (−1 V vs Hg_2/Hg_2Cl_2) upon TMA-POSS addition. These results collectively validate the remarkable inhibitory effect of TMA-POSS on side reactions.

The nucleation and growth behaviors of Zn were investigated via chronoamperometry (CA). At an overpotential of −150 mV, the ZS electrolyte exhibits a continuous increase in current density over time (Figure 4f), revealing laterally dominant Zn^{2+} diffusion across the electrode surface, which is consistent with a 2D diffusion-controlled nucleation process [55]. This process causes heterogeneous Zn nucleation and dendrite formation. In sharp contrast, the ZS/TMA-POSS electrolyte undergoes a significantly shortened 2D diffusion duration before transitioning to a more stable 3D diffusion, suggesting the formation of finer, more uniform Zn seeds during the initial nucleation stage [56], which facilitate uniform and dense Zn deposition. In the electrolyte, Zn^{2+} predominantly exists as $[Zn(H_2O)_6]^{2+}$, and its desolvation represents the primary kinetic barrier for Zn^{2+} transport and Zn deposition [55]. The desolvation capability of $[Zn(H_2O)_6]^{2+}$ is commonly evaluated through Arrhenius activation energy (E_a) derived from the Arrhenius equation [57]. As shown in Figure 4g, the ZS/TMA-POSS electrolyte exhibits a substantially lower E_a (27.96 kJ mol^{-1}) compared to the ZS electrolyte (42.45 kJ mol^{-1}), demonstrating that $T_8(Si\text{-}O)_8^{8-}$ facilitates $[Zn(H_2O)_6]^{2+}$ desolvation via nanoconfinement effects and reconfigured solvation structures. This enhanced desolvation kinetics accelerates both Zn^{2+} transport and Zn deposition. Electrochemical impedance spectroscopy (EIS) reveals significantly reduced charge transfer resistance (R_{ct}) across different temperatures, aligning with the E_a trend and further confirming improved interfacial Zn^{2+} transport (Figure S14).

As mentioned before, $T_8(Si\text{-}O)_8^{8-}$ features an Si−O−Si framework with a precisely defined pore size larger than Zn^{2+} (1.48 Å) but smaller than SO_4^{2-} (5.9 Å) and $[Zn(H_2O)_6]^{2+}$ (8.6 Å). This architecture facilitates $[Zn(H_2O)_6]^{2+}$ desolvation, enhances Zn^{2+} transport, and blocks SO_4^{2-} migration through nanoconfinement effect. Meanwhile, the Si−O−Si nanocage also restricts SO_4^{2-} diffusion through electrostatic interactions and limits H_2O penetration due to its inherent hydrophobicity. These synergistic effects significantly inhibit space charge layer formation, modulate Zn deposition, and eliminate interfacial reactive H_2O, thereby suppressing side reactions and promoting dense Zn deposition. As shown in Figure 4h and Figure S15, a high Zn^{2+} transference number ($t_{Zn^{2+}}$) of up to 0.77 is observed for the ZS/TMA-POSS electrolyte, significantly higher than that of the ZS electrolyte (0.35), demonstrating enhanced Zn^{2+} transport and effective suppression of SO_4^{2-} migration [58]. The sluggish Zn^{2+} diffusion kinetics and limited interfacial Zn^{2+} replenishment in ZS electrolyte fundamentally constrain the rate performance of Zn//Zn symmetric cells [59], leading to cell failure when current densities exceed 10 mA cm^{-2}. In contrast, Zn//Zn cells using ZS/TMA-POSS electrolyte demonstrate smaller voltage hysteresis and admirable cycling stability across a wide range of current densities (1–30 mA cm^{-2}), exhibiting superior rate performance. Notably, the polarization voltage returns to its initial level upon reducing the current density to 1 mA cm^{-2}, confirming high electrochemical reversibility (Figure 4j). The dynamic protective behavior of TMA-POSS is evidenced by the evolution of the exchange current density (j_0). j_0 has been utilized to evaluate the dynamic evolution of interfacial Zn^0/Zn^{2+} redox reaction during battery cycling [31, 60, 61]. Symmetrical cells were subjected to repeated rate performance tests, and the measured overpotentials were used to calculate the j_0 for each rate cycle via the Butler-Volmer equation (Equation S11). As illustrated in Figure 4i, the ZS/TMA-POSS electrolyte exhibits a higher j_0 than that of the ZS electrolyte, indicating the capacity of TMA-POSS to dynamically stabilize Zn plating/stripping processes [59].

The effects of TMA-POSS on Zn plating/stripping behavior were systematically investigated using Zn//Cu asymmetric cells. Cyclic voltammetry (CV) (Figure 4k) demonstrates that the nucleation overpotential of the ZS/TMA-POSS electrolyte is higher than that of the ZS electrolyte ($|AA'| = 13$ mV). An elevated nucleation overpotential tends to promote the formation of finer Zn seeds [62], indicating that TMA-POSS induces the formation of numerous fine nuclei during the initial nucleation stage. This optimized nucleation behavior facilitates subsequent uniform crystal growth, thereby enabling dense Zn deposition. Additionally, the initial Zn plating voltage profiles obtained from the Zn//Cu cell (Figure S16) also show an increased nucleation overpotential, consistent with the CV results. The optimized nucleation behavior arises from the electrostatic shielding effect imparted by the TMA^+ layer and the uniform interfacial electric field/Zn^{2+} flux enabled by the $T_8(Si\text{-}O)_8^{8-}$ layer, which to a certain extent retards the kinetics of initial Zn^{2+} deposition, but significantly accelerates the subsequent electrodeposition growth process [63–65]. This kinetic modulation drives the thermodynamically favorable homogeneous nucleation and growth of small Zn nuclei [5].

Zn//Zn symmetric cells enable quantitative evaluation of Zn anode reversibility through galvanostatic plating/stripping. The

influence of TMA-POSS concentration on Zn anode stability was systematically investigated under fixed condition of 7 mA cm^{-2}, 3.5 mAh cm^{-2}. Low concentrations provide insufficient $T_8(Si\text{-}O)_8^{8-}/TMA^+$ coverage, failing to sufficiently mitigate side reactions and suppress dendrite growth. Conversely, excessive TMA-POSS compromise Zn^{2+} transport and deposition kinetics due to interfacial overaccumulation of TMA^+, leading to degraded cell performance. As shown in Figure S17, both insufficient and excessive TMA-POSS concentration fails to achieve satisfactory cycling stability. At the optimized concentration (10 mM), the Zn//Zn cell exhibits exceptional cycling stability over 4700 h at 1 mA cm^{-2}, 0.5 mAh cm^{-2}, far exceeding the ZS electrolyte, which short-circuited after only 55 h (Figure 5a). Under harsh condition (10 mA cm^{-2}, 5 mAh cm^{-2}), the cell with ZS/TMA-POSS electrolyte maintains stable cycling for 825 h (Figure 5b). These performances outperform those of most reported additives (Figure S18), demonstrating remarkable reversibility. Notably, deep discharge tests at 20 mA cm^{-2}, 10 mAh cm^{-2} (DOD = 17%) and at 1 mA cm^{-2}, 30 mAh cm^{-2} (DOD = 51.3%) reveal stable Zn plating/stripping cycles exceeding 270 and 500 h, respectively, outperforming most reported additives featuring electrostatic shielding capabilities. Furthermore, cost analysis further reveals that TMA-POSS offers a significant economic advantage over conventional electrostatic shielding additives, highlighting its practical potential (Figures S19–S21).

Coulombic efficiency (CE) is a crucial indicator for evaluating the stability and reversibility of Zn anode. As shown in Figure 5c, the Zn//Cu asymmetric cell using the ZS/TMA-POSS electrolyte achieves long-term cycling stability over 2110 cycles (1 mA cm^{-2}, 0.5 mAh cm^{-2}), with an impressive CE of 99.2%. The corresponding capacity-voltage profile shows highly reversible plating/stripping behavior (Figure 5e). In sharp contrast, due to dendrite formation and harmful side reactions, the cell using the ZS electrolyte undergoes abrupt short-circuiting after merely 75 cycles (Figure 5d), further confirming the significantly enhanced reversibility of the Zn anode. Notably, the cyclic evolution of Zn nucleation overpotentials in Zn//Cu cells was systematically investigated using CV. As shown in Figure 5f, the ZS/TMA-POSS electrolyte enables rapid stabilization of nucleation overpotential (17–20 mV) after the second cycle, whereas the ZS electrolyte exhibits lower but highly fluctuating overpotentials throughout cycling. This distinct behavior indicates that TMA-POSS stabilizes Zn nucleation and promotes the formation of finer and more uniform Zn seeds, also suggesting a more homogeneous ion concentration and electric field distributions at the Zn anode surface. Additionally, no additional redox current responses are observed in all CV curves of the ZS/TMA-POSS cell (Figure S22), and the ^1H NMR spectra of the ZS/TMA-POSS electrolyte before and after cycling (Figure S23) show nearly identical chemical shifts, peak shapes, and relative integral intensities, with no discernible degradation peaks or loss of characteristic signals [66, 67]. This result directly confirms the electrochemical inertness of TMA-POSS and its non-sacrificial nature during Zn plating/stripping processes. To further validate the dynamic repair functionality of TMA-POSS, a Zn//Cu battery was assembled using an electrolytic cell and carried out CV measurements. In the ZS electrolyte, the nucleation overpotential progressively decreases with cycling, whereas the introduction of TMA-POSS at the sixth cycle immediately elevates and stabilizes the nucleation overpotential, directly confirming the dynamic repair capability of TMA-POSS (Figure S24).

The influence of TMA-POSS on Zn deposition morphology was further investigated. Scanning electron microscope (SEM) images of Zn anodes after 50 cycles at 1, 5, and 10 mA cm^{-2} (with corresponding deposition capacities of 0.5, 2.5, and 5 mAh cm^{-2}) show that Zn deposits as randomly oriented hexagonal nanoflakes in ZS electrolyte, exhibiting a loosely packed morphology and substantial accumulation of by-products (Figure 6a). Poor interfacial adhesion promotes detachment of these nanoflakes and the formation of "dead Zn," while by-products impede interfacial mass transfer and accelerate anode surface roughening, severely compromising anode stability [68]. In contrast, the ZS/TMA-POSS electrolyte yields a smooth, dendrite-free surface with no detectable by-products. Even under the extreme condition of 10 mA cm^{-2}, 5 mAh cm^{-2}, the Zn anode retains a flat and densely compacted morphology (Figure 6b). These observations demonstrates that TMA-POSS effectively regulates interfacial Zn^{2+}/SO_4^{2-} transport and excludes free H_2O from the interface, thereby suppressing side reactions and enabling dendrite-free deposition. In-situ optical microscopy (Figure S25) reveals that the electrode in the ZS electrolyte begins releasing gas within 10 min, accompanied by uneven Zn plating. As plating continues, dendrite growth and gas evolution become increasingly pronounced (Figure 6c). In contrast, the ZS/TMA-POSS electrolyte maintains stable, bubble-free plating with dense Zn deposition throughout the plating process (Figure 6e). 3D Laser confocal scanning microscopy (3D LCSM) (Figure 6d and Figure S26a,b) reveals severe surface roughening of the Zn anode cycled in the ZS electrolyte, characterized by numerous protrusions and pits (maximum altitude: 62.9 μm). In contrast, the Zn anode cycled in the ZS/TMA-POSS electrolyte maintains a smooth surface, with the maximum altitude significantly reduced to 17.6 μm, indicating superior deposition behavior (Figure 6f and Figure S26c,d). These results validate that the $T_8(Si\text{-}O)_8^{8-}/TMA^+$ interface effectively suppresses space charge layer-induced dendrite growth through regulation of interfacial Zn^{2+}/SO_4^{2-} transport [11] and guides dense Zn deposition. Furthermore, the scratch healing behavior on the Zn anode surface was monitored by optical microscopy. As shown in Figure 6g, scratches exhibit substantial recovery after only 1 h of cycling in the ZS/TMA-POSS electrolyte and are nearly fully healed after 7 h. In contrast, the scratches remain clearly visible after 17 h of cycling in the ZS electrolyte (Figure S27), clearly demonstrating the dynamic self-healing capability of TMA-POSS.

2.4 | Full-Cell Performance Characterization

To evaluate the practical applicability of TMA-POSS additive, $Zn//MnO_2$ full cells were assembled using 2 M $ZnSO_4$ + 0.1 M $MnSO_4$ or 2 M $ZnSO_4$ + 0.1 M $MnSO_4$ + 10 mM TMA-POSS as electrolytes [69]. The MnO_2 and V_2O_5 cathodes were synthesized according to previously reported methods [69, 70], and their successful preparation was verified by XRD (Figures S28 and S29). CV curves (Figure 7a) display similar redox peaks, indicating that TMA-POSS does not participate in the electrochemical reactions of the full cell and thus acts in a non-sacrificial manner. Moreover, TMA-POSS enlarges the current response area and reduces the redox peak potential separation, suggesting improved Zn storage

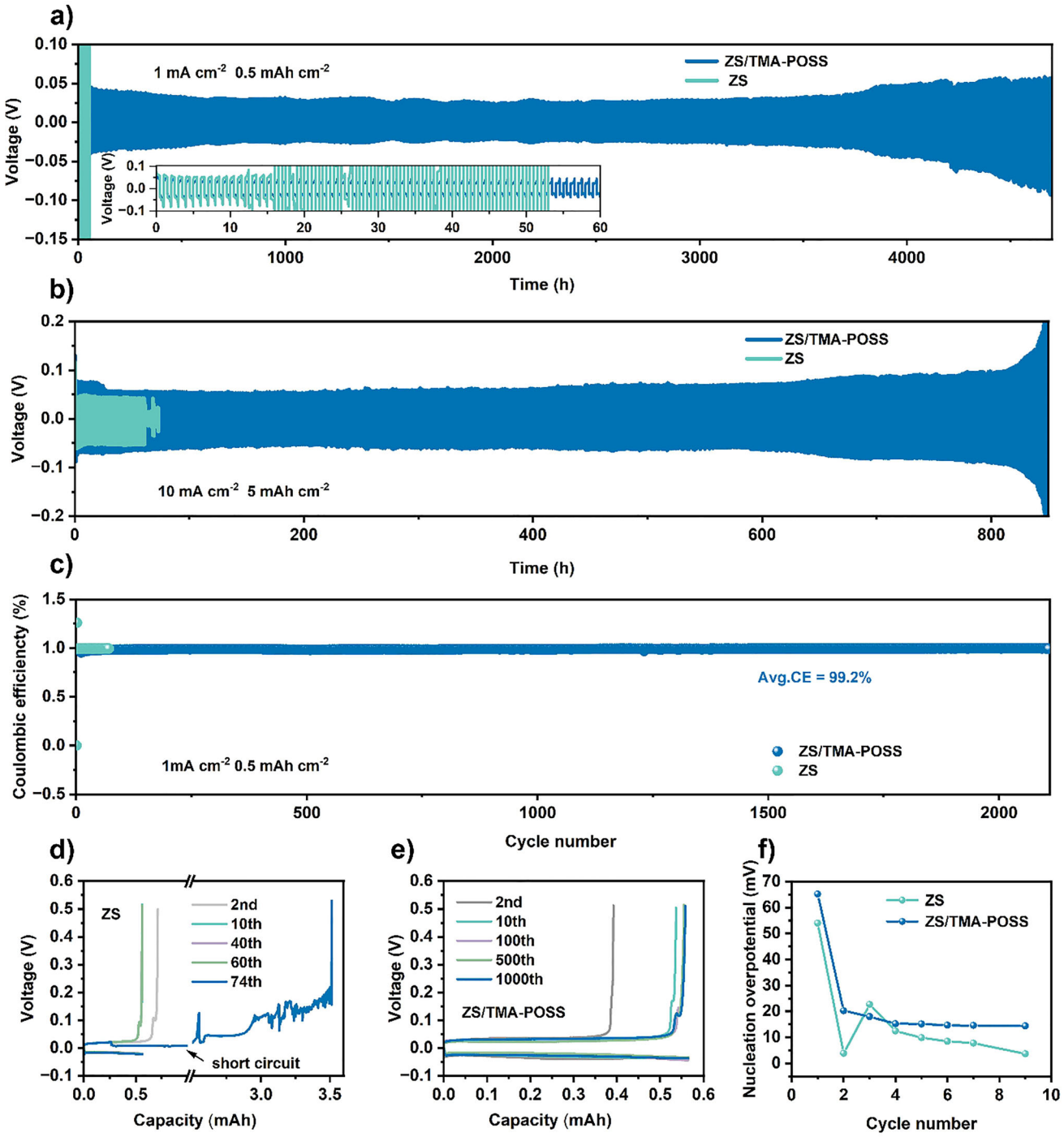

FIGURE 5 | Cycling performance of Zn//Zn cells at a) 1 mA cm^{-2}, 0.5 mAh cm^{-2} and b) 10 mA cm^{-2}, 5 mAh cm^{-2}. c) The Coulombic efficiency of the Zn//Cu cell at 1 mA cm^{-2}, 0.5 mAh cm^{-2}. d) Capacity–voltage curves of ZS electrolyte with different cycles. e) Capacity–voltage curves of ZS/TMA-POSS electrolyte with different cycles. f) Nucleation overpotential evolution of Zn//Cu cell at different cycle numbers.

capacity and accelerated electrochemical reaction kinetics [71]. Figure 7b shows that the cell with ZS/TMA-POSS electrolyte delivers higher specific capacities across various current densities, demonstrating superior rate performance. Notably, upon returning the current density to 0.5 A g^{-1}, the corresponding charge/discharge plateaus exhibit reduced voltage hysteresis (Figure 7c), indicating that TMA-POSS effectively mitigates battery polarization [72]. The improved reaction kinetics and energy storage efficiency are primarily attributed to reduced charge-transfer resistance and optimized Zn^{2+} transport. This is corroborated by electrochemical impedance spectroscopy (EIS) results (Figure S30), which show that TMA-POSS remarkably reduces the impedance of the Zn//MnO_2 cell from 360.7 to 123.6 Ω [38]. Collectively, the above results demonstrate that TMA-POSS effectively suppresses side reactions and stabilizes the Zn anode/electrolyte interface, thereby reducing passivation and enhancing electrochemical kinetics. Through synergistic interfacial stabilization and regulation of Zn^{2+}/SO_4^{2-} migration,

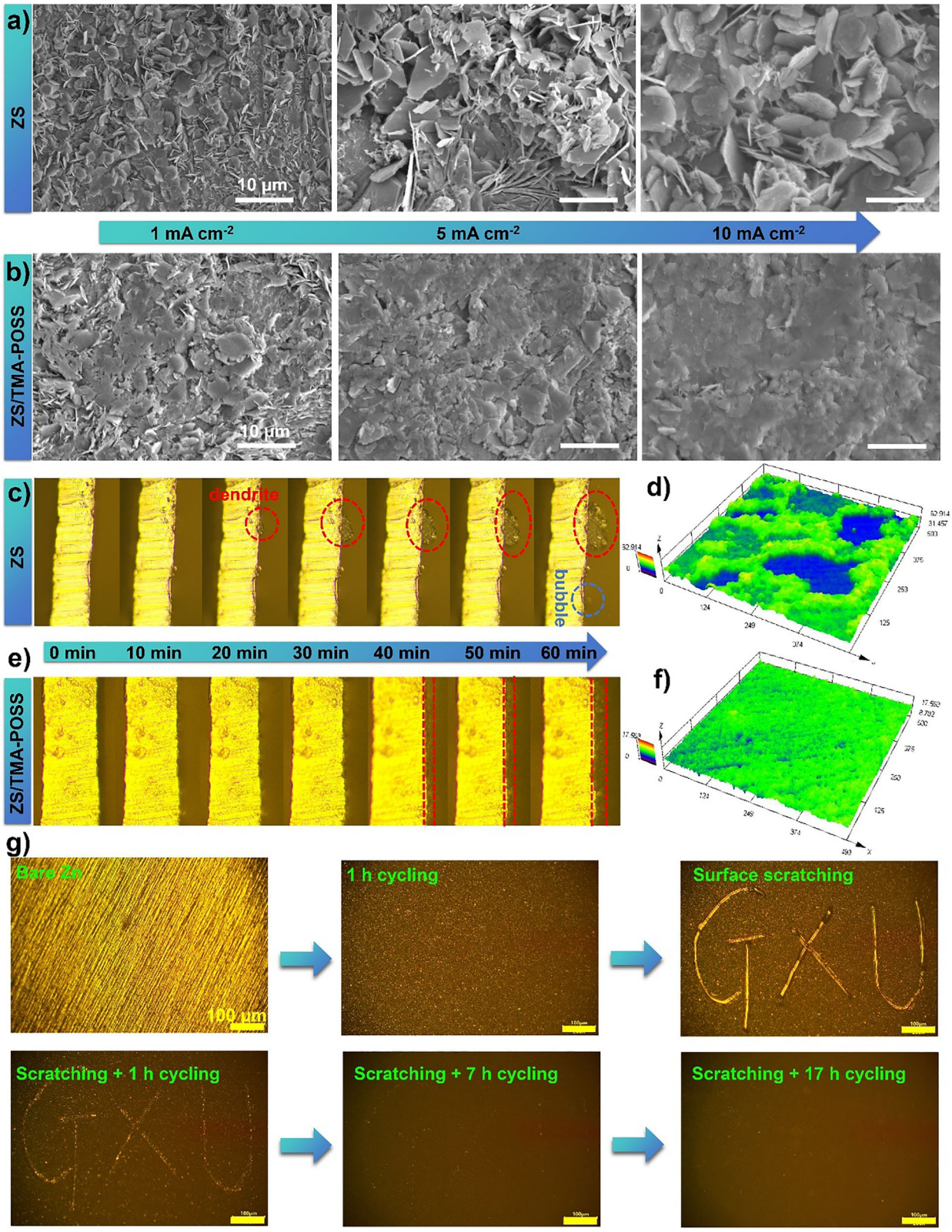

FIGURE 6 | SEM images of Zn deposition morphology in a) ZS and b) ZS/TMA-POSS electrolytes with various area capacities of 0.5, 2.5, and 5 mAh cm^{-2}, respectively. In situ optical microscopy images of Zn deposition morphology at 10 mA cm^{-2} in c) ZS and e) ZS/TMA-POSS electrolytes. 3D CLSM images of Zn deposition morphology in d) ZS and f) ZS/TMA-POSS electrolytes. g) The self-healing process of scratches on the Zn anode by TMA-POSS.

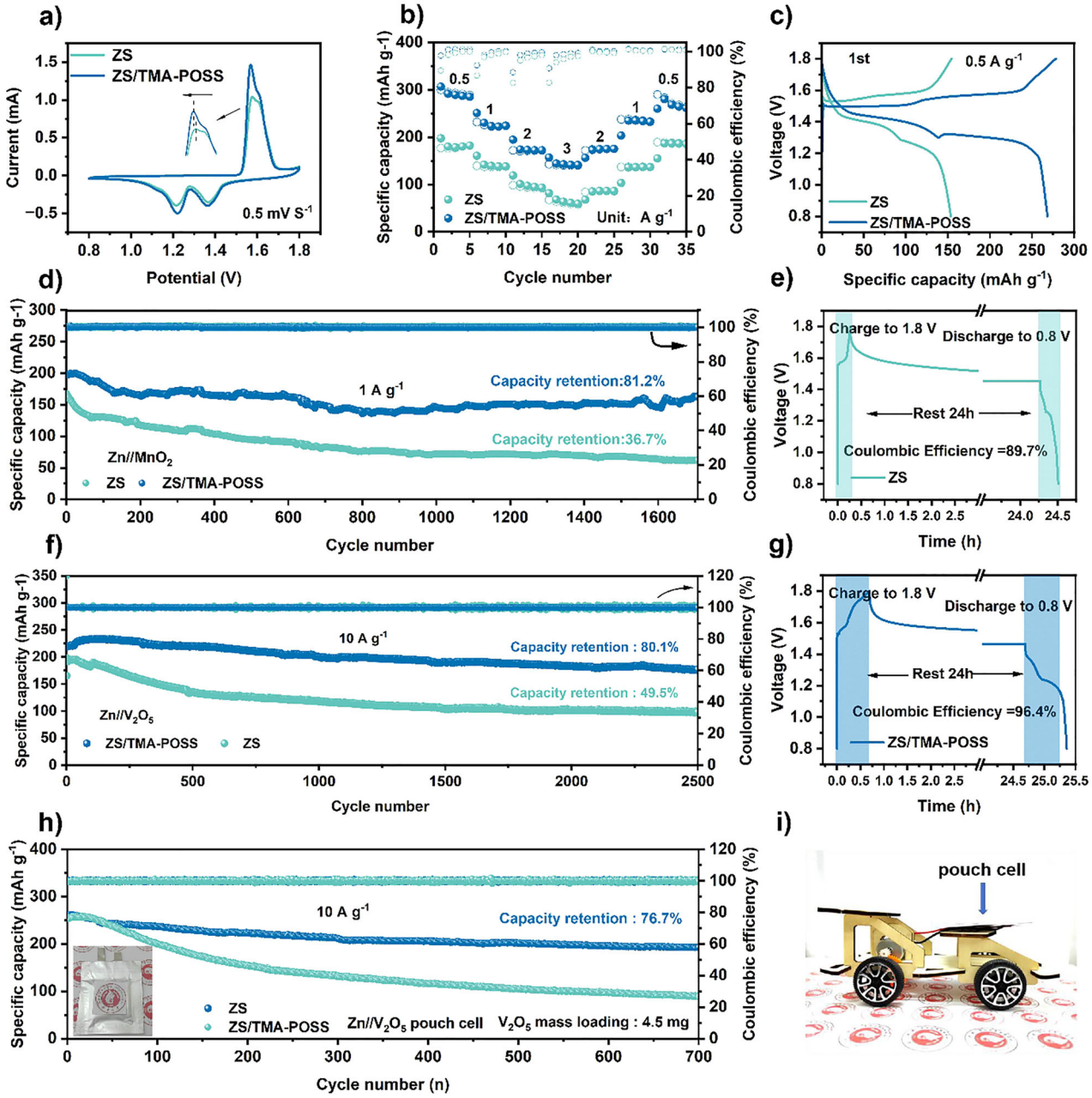

FIGURE 7 | Electrochemical performance of Zn//MnO_2 full cells: a) CV curves at 0.5 mV s^{-1}, b) rate performance at different current densities, (c) the corresponding charge/discharge curves, d) cycling performance at 1 A g^{-1}, self-discharge curves with e) ZS and g) ZS/TMA-POSS electrolytes. f) Cycling performance of Zn//V_2O_5 full cells at 10 A g^{-1}. h) Cycling performance of Zn//V_2O_5 pouch cell at 10 A g^{-1} with ZS/TMA-POSS electrolyte. i) Digital photograph of a Zn//V_2O_5 pouch cell powering a toy car.

TMA-POSS enables exceptional long-term cycling stability for the Zn//MnO_2 full cell: after 1700 cycles at 1 A g^{-1}, the cell with ZS/TMA-POSS electrolyte retains 81.2% of its initial capacity (from 198.1 to 160.9 mAh g^{-1}), far exceeding the 36.7% retention for the ZS electrolyte (Figure 7d). Additionally, self-discharge is a crucial indicator for rechargeable aqueous batteries [72]. The cell with ZS/TMA-POSS electrolyte delivers 96.4% capacity retention after 24 h of rest, significantly higher than the 89.7% retention observed for the ZS-based cell (Figure 7e,g), further confirming the effectiveness of TMA-POSS in suppressing side reactions.

The superior electrochemical performance of the Zn//V_2O_5 full cell highlights the broad applicability of TMA-POSS in cathode materials. Likewise, as illustrated in Figure S31, the impedance of the Zn//V_2O_5 full cell decreases significantly from 350.8 to 103.2 Ω upon introducing TMA-POSS. The cell employing the ZS/TMA-POSS electrolyte delivers higher specific capacities over a current density range of 0.5 to 10 A g^{-1} and retains a capacity of 197.6 mAh g^{-1} when the current density switches back to 5 A g^{-1}, demonstrating superior rate performance (Figures S32 and S33). These improvements in reaction kinetics and energy storage efficiency confirm that TMA-POSS effectively suppresses side

reactions and stabilizes the Zn anode interface. Figure 7f shows the exceptional cycling stability of the Zn//V_2O_5 full cell with the ZS/TMA-POSS electrolyte, delivering a high capacity retention of 80.1% after 2500 cycles at 10 A g^{-1}. In sharp contrast, the cell with the ZS electrolyte exhibits rapid capacity decay, retaining merely 49.5% of its initial capacity after cycling. Furthermore, TMA-POSS demonstrates a notable inhibitory effect on the self-discharge performance of the Zn//V_2O_5 full cell (Figure S34). Ultimately, the practical application of the TMA-POSS additive was further evaluated using Zn//V_2O_5 pouch cell comprising a V_2O_5-coated graphene cathode (electrode size: 3 cm × 3 cm; V_2O_5 loading: 4.5 mg cm^{-2}), a Zn metal anode, and the ZS/TMA-POSS electrolyte, which delivers stable power output and excellent cycling stability over 800 cycles (Figure 7h). Moreover, the pouch cell can successfully power a toy car, highlighting the practical potential of TMA-POSS (Figure 7i and Video S1).

3 | Conclusion

In summary, we have developed a novel self-adaptive dual-ion interface using multifunctional, non-sacrificial TMA-POSS additive. DFT, MD and multiphysics simulations combined with experimental results confirm that TMA-POSS spontaneously self-assembles into a well-defined $T_8(Si\text{-}O)_8^{8-}$/TMA^+ bilayer structure on the Zn surface. The inner TMA^+ layer promotes homogeneous Zn nucleation and dense Zn deposition through electrostatic shielding effect. The outer $T_8(Si\text{-}O)_8^{8-}$ layer, featuring a precisely ordered topological architecture, regulates the transport of Zn^{2+} and SO_4^{2-} via nanoconfinement effects and electrostatic interactions while simultaneously blocking H_2O penetration, thereby effectively suppressing space charge layer formation and side reactions. Besides, the resulting self-assembled dual-ion interface exhibits high structural stability and dynamic adaptability under prolonged cycling conditions. As a result, this novel dynamic self-adaptive dual-ion stabilization mechanism endows the Zn anode with outstanding reversibility. Zn//Zn symmetric cells achieve long cycling life exceeding 4700 h (1 mA cm^{-2}, 0.5 mAh cm^{-2}) and 850 h (10 mA cm^{-2}, 5 mAh cm^{-2}). Even under a high DOD of 51.35%, it still maintains stable operation for 500 h. Zn//Cu asymmetric cell retains a high coulombic efficiency of 99.6% over 2110 cycles at 1 mA cm^{-2}, 0.5 mAh cm^{-2}. For practical application, Zn//MnO_2 and Zn//V_2O_5 full cells deliver outstanding capacity retentions of 81.2% (after 1700 cycles, 1 A g^{-1}) and 80.1% (after 2500 cycles, 10 A g^{-1}). This cost-effective, non-sacrificial additive strategy provides a practical approach for designing advanced functional additives, and opens new avenues toward the commercialization of high-stability and reliable AZIBs.

Acknowledgements

This work was supported by the National Natural Science Foundation of China (22578083, 22308066), Natural Science Foundation of Guangxi Province (2025JJB160015), Guangxi University Young and Middle-aged Teachers in Science Research Basic Capability Enhancement Project (2024KY0027).

Funding

This work was supported by the National Natural Science Foundation of China (22578083, 22308066), Natural Science Foundation of Guangxi Province (2025JJB160015), Guangxi University Young and Middle-aged Teachers in Science Research Basic Capability Enhancement Project (2024KY0027).

Conflicts of Interest

The authors declare no conflict of interest.

Data Availability Statement

The data that support the findings of this study are available from the corresponding author upon reasonable request.

References

1. D. Chao, W. Zhou, F. Xie, et al., "Roadmap for Advanced Aqueous Batteries: From Design of Materials to Applications," *Science Advances* 6 (2020): aba4098, https://doi.org/10.1126/sciadv.aba4098.

2. J. Hao, X. Li, X. Zeng, D. Li, J. Mao, and Z. Guo, "Deeply Understanding the Zn Anode Behaviour and Corresponding Improvement Strategies in Different Aqueous Zn-Based Batteries," *Energy & Environmental Science* 13 (2020): 3917–3949, https://doi.org/10.1039/d0ee02162h.

3. Z. Liu, Y. Huang, Y. Huang, et al., "Correction: Voltage Issue of Aqueous Rechargeable Metal-Ion Batteries," *Chemical Society Reviews* 49 (2020): 643–644, https://doi.org/10.1039/c9cs90105a.

4. J.-L. Yang, P. Yang, T. Xiao, and H. J. Fan, "Designing Single-Ion Conductive Electrolytes for Aqueous Zinc Batteries," *Matter* 7 (2024): 1928–1949, https://doi.org/10.1016/j.matt.2024.03.014.

5. Y. Chen, S. Zhou, J. Li, et al., "Tuning Zn^{2+} Deposition Kinetics towards Deep-Reversible Zinc Metal Batteries with all-Climate Adaptability," *Angewandte Chemie International Edition* 64 (2025): 20242325, https://doi.org/10.1002/anie.202423252.

6. D. Han, Z. Wang, H. Lu, et al., "A Self-Regulated Interface toward Highly Reversible Aqueous Zinc Batteries," *Advanced Energy Materials* 12 (2022): 2102982, https://doi.org/10.1002/aenm.202102982.

7. X. Liu, H. Li, J. Liang, J. Yin, Z. Li, and Z. Lu, "Advancing Highly Reversible Zinc Electrode: Principles and Strategies for Electron and Ion Transport Kinetics Regulation," *Energy Storage Materials* 81 (2025): 104446, https://doi.org/10.1016/j.ensm.2025.104446.

8. R. Wang, S. Luo, Y. Guo, et al., "Synergistic Modulation of Zn Anode via Ferroelectric and Zincophilic Cr-Doped ZnO Interface," *Advanced Functional Materials* 35 (2025): 2503892, https://doi.org/10.1002/adfm.202503892.

9. S. Chen, D. Ji, Q. Chen, J. Ma, S. Hou, and J. Zhang, "Coordination Modulation of Hydrated Zinc Ions to Enhance Redox Reversibility of Zinc Batteries," *Nature Communications* 14 (2023): 3526, https://doi.org/10.1038/s41467-023-39237-3.

10. H. Li, S. Li, R. Hou, et al., "Recent Advances in Zinc-Ion Dehydration Strategies for Optimized Zn–Metal Batteries," *Chemical Society Reviews* 53 (2024): 7742–7783, https://doi.org/10.1039/d4cs00343h.

11. J. Lin, C. Ji, G. Guo, et al., "Interfacial H-Bond Network/Concentration Fields/Electric Fields Regulation Achieved by D-Valine Anions Realizes the Highly Efficient Aqueous Zinc Ion Batteries," *Angewandte Chemie International Edition* 64 (2025): 202501721, https://doi.org/10.1002/anie.202501721.

12. J. Yang, B. Yin, Y. Sun, et al., "Zinc Anode for Mild Aqueous Zinc-Ion Batteries: Challenges, Strategies, and Perspectives," *Nano-Micro Letters* 14 (2022): 42, https://doi.org/10.1007/s40820-021-00782-5.

13. H. Bian, C. Li, G. Xue, et al., "Smart Self-Healing Anode/Electrolyte Interphases for Stabilizing Zn Anode," *Advanced Materials* 37 (2025): 2505982, https://doi.org/10.1002/adma.202505982.

14. J. N. Chazalviel, "Electrochemical Aspects of the Generation of Ramified Metallic Electrodeposits," *Physical Review A* 42 (1990): 7355–7367, https://doi.org/10.1103/physreva.42.7355.

15. J.-N. C. V. Flew-y, M. Ross, and B. Sapoval, "The Role of the Anions in the Growth Speed of Fractal Electrodeposits," *Journal of Electroanalytical Chemistry and Interfacial Electrochemistry* 290 (1990): 249–255, https://doi.org/10.1016/0022-0728(90)87434-L.

16. Z. Wen, Z. Hu, X. Wang, et al., "Weakening the Space Charge Layer Effect through Tethered Anion Electrolyte and Piezoelectric Effect toward Ultra-Stable Zinc Anode," *Advanced Materials* 36 (2024): 2407390, https://doi.org/10.1002/adma.202407390.

17. J. Xu, H. Li, Y. Jin, et al., "Understanding the Electrical Mechanisms in Aqueous Zinc Metal Batteries: From Electrostatic Interactions to Electric Field Regulation," *Advanced Materials* 36 (2023): 2309726, https://doi.org/10.1002/adma.202309726.

18. H. Huang, J. Xu, Y. Huang, et al., "Adjusting Interface Dynamics: a New Insight into the Role of Electrolyte Additive in Facilitating Highly Reversible (002)-Textured Zinc Anode at High Current and Areal Densities," *Advanced Energy Materials* 14 (2024): 2401643, https://doi.org/10.1002/aenm.202401643.

19. G. Guo, C. Ji, J. Lin, et al., "Interfacial Domino Effect Triggered by β-Alanine Cations Realized Highly Reversible Zinc-Metal Anodes," *Angewandte Chemie International Edition* 63 (2024): 202407417, https://doi.org/10.1002/anie.202407417.

20. M. Qiu, P. Sun, Y. Wang, L. Ma, C. Zhi, and W. Mai, "Anion-Trap Engineering toward Remarkable Crystallographic Reorientation and Efficient Cation Migration of Zn Ion Batteries," *Angewandte Chemie International Edition* 61 (2022): 202210979, https://doi.org/10.1002/anie.202210979.

21. J. Ji, Z. Zhu, H. Du, et al., "Zinc-Contained Alloy as a Robustly Adhered Interfacial Lattice Locking Layer for Planar and Stable Zinc Electrodeposition," *Advanced Materials* 35 (2023): 2211961, https://doi.org/10.1002/adma.202211961.

22. D. Li, L. Cao, T. Deng, S. Liu, and C. Wang, "Design of a Solid Electrolyte Interphase for Aqueous Zn Batteries," *Angewandte Chemie International Edition* 60 (2021): 13035–13041, https://doi.org/10.1002/anie.202103390.

23. Q. Zhang, J. Luan, Y. Tang, X. Ji, and H. Wang, "Interfacial Design of Dendrite-Free Zinc Anodes for Aqueous Zinc-Ion Batteries," *Angewandte Chemie International Edition* 59 (2020): 13180–13191, https://doi.org/10.1002/anie.202000162.

24. Y. Wang, Z. Wang, F. Yang, et al., "Electrolyte Engineering Enables High Performance Zinc-Ion Batteries," *Small* 18 (2022): 2107033, https://doi.org/10.1002/smll.202107033.

25. Y. Wu, Z. Zhu, D. Shen, et al., "Electrolyte Engineering Enables Stable Zn-Ion Deposition for Long-Cycling Life Aqueous Zn-Ion Batteries," *Energy Storage Materials* 45 (2022): 1084–1091, https://doi.org/10.1016/j.ensm.2021.11.003.

26. Q. Zhang, Y. Ma, Y. Lu, et al., "Modulating Electrolyte Structure for Ultralow Temperature Aqueous Zinc Batteries," *Nature Communications* 11 (2020): 4463, https://doi.org/10.1038/s41467-020-18284-0.

27. Y. Pan, Z. Zuo, Y. Jiao, and P. Wu, "Constructing Lysozyme Protective Layer via Conformational Transition for Aqueous Zn Batteries," *Advanced Materials* 36 (2024): 2314144, https://doi.org/10.1002/adma.202314144.

28. Z. Peng, H. Yan, Q. Zhang, et al., "Stabilizing Zinc Anode through Ion Selection Sieving for Aqueous Zn-Ion Batteries," *Nano Letters* 24 (2024): 9137–9146, https://doi.org/10.1021/acs.nanolett.4c00693.

29. J. Wei, P. Zhang, J. Sun, et al., "Advanced Electrolytes for High-Performance Aqueous Zinc-Ion Batteries," *Chemical Society Reviews* 53 (2024): 10335–10369, https://doi.org/10.1039/d4cs00584h.

30. Q. Wu, J. Huang, J. Zhang, et al., "Multifunctional Cellulose Nanocrystals Electrolyte Additive Enable Ultrahigh-Rate and Dendrite-Free Zn Anodes for Rechargeable Aqueous Zinc Batteries," *Angewandte Chemie International Edition* 63 (2024): 202319051, https://doi.org/10.1002/anie.202319051.

31. Q. Wu, J. Zhang, S. Yang, et al., "Bridging Electrolyte Bulk and Interfacial Chemistry: Dynamic Protective Strategy Enable Ultra-Long Lifespan Aqueous Zinc Batteries," *Angewandte Chemie International Edition* 64 (2024): 202418524, https://doi.org/10.1002/anie.202418524.

32. Ł. John and J. Ejfler, "A Brief Review on Selected Applications of Hybrid Materials Based on Functionalized Cage-Like Silsesquioxanes," *Polymers* 15, no. 6 (2023): 1452, https://doi.org/10.3390/polym15061452.

33. M. Nowacka and A. Kowalewska, "Self-Healing Silsesquioxane-Based Materials," *Polymers* 14, no. 9 (2022): 1869, https://doi.org/10.3390/polym14091869.

34. S. Liu, R. Guo, C. Li, et al., "POSS Hybrid Hydrogels: a Brief Review of Synthesis, Properties and Applications," *European Polymer Journal* 143 (2021): 110180, https://doi.org/10.1016/j.eurpolymj.2020.110180.

35. C. Yan, L. Zhu, P. Li, et al., "Multi-Level Zn^{2+} -Buffering Interphase Enabled by Hierarchical Nanostructure Engineering of Gel Polymers for Highly Reversible Zinc Metal Anode," *Advanced Materials* 38 (2025): 15316, https://doi.org/10.1002/adma.202515316.

36. W. Zhong, H. Cheng, S. Zhang, et al., "Cation-Driven Phase Transition and Anion-Enhanced Kinetics for High Energy Efficiency Zinc-Interhalide Complex Batteries," *Nature Communications* 16 (2025): 4586, https://doi.org/10.1038/s41467-025-59894-w.

37. J. He, Y. Tang, G. Liu, et al., "Intrinsic Hydrogen-Bond Donors-Lined Organophosphate Superionic Nanochannels Levering High-Rate-Endurable Aqueous Zn Batteries," *Advanced Energy Materials* 12 (2022): 2202661, https://doi.org/10.1002/aenm.202202661.

38. N. Hu, W. Lv, W. Chen, et al., "A Double-Charged Organic Molecule Additive to Customize Electric Double Layer for Super-Stable and Deep-Rechargeable Zn Metal Pouch Batteries," *Advanced Functional Materials* 34 (2024): 2311773, https://doi.org/10.1002/adfm.202311773.

39. R. Wang, J. Zhu, M. Yang, and Z. Niu, "Simultaneous Manipulation of Anions and Water Molecules by Lewis Acid–Base for Highly Stable Zn Anodes," *Angewandte Chemie International Edition* 64 (2025): 202501327, https://doi.org/10.1002/anie.202501327.

40. Q. Kang, H. Liang, Z. Zhu, et al., "Non-Substituted Aromatic Pyridine N-Oxide Additives with an Intrinsic N→O Acceptor for Ultra-Long-Life Zn||MnO_2 Batteries," *Angewandte Chemie International Edition* 64 (2025): 202420183, https://doi.org/10.1002/anie.202420183.

41. H. Yu, D. Chen, Q. Li, et al., "In Situ Construction of Anode–Molecule Interface via Lone-Pair Electrons in Trace Organic Molecules Additives to Achieve Stable Zinc Metal Anodes," *Advanced Energy Materials* 13 (2023): 2300550, https://doi.org/10.1002/aenm.202300550.

42. Q. Zong, R. Li, J. Wang, Q. Zhang, and A. Pan, "Tailoring the Whole Deposition Process from Hydrated Zn^{2+} to Zn 0 for Stable and Reversible Zn Anode," *Angewandte Chemie International Edition* 63 (2024): 202409957, https://doi.org/10.1002/anie.202409957.

43. H. Sun, N. Cai, X. Bai, et al., "Dendrite-Free Zn Anode Enabled by Dual-Function Itaconic Acid Electrolyte Additive via Controllable Acidic Environment and in Situ Interfacial Protective Layer for Durable Aqueous Zinc Ion Batteries," *Advanced Functional Materials* 35 (2025): 2424398, https://doi.org/10.1002/adfm.202424398.

44. M. Liu, Y. Wang, Y. Li, et al., "Dual-Functional Interfacial Layer Enabled by Gating-Shielding Effects for Ultra-Stable Zn Anode," *Advanced Materials* 36 (2024): 2406145, https://doi.org/10.1002/adma.202406145.

45. H. Wang, H. Du, R. Zhao, et al., "Stable Zn Metal Anodes Enabled by Restricted Self-Diffusion via Succinimide Surfactant," *Advanced Functional Materials* 33 (2023): 2213803, https://doi.org/10.1002/adfm.202213803.

46. F. Ling, L. Wang, F. Liu, et al., "Multi-Scale Structure Engineering of $ZnSnO_3$ for Ultra-Long-Life Aqueous Zinc-Metal Batteries," *Advanced Materials* 35 (2023): 2208764, https://doi.org/10.1002/adma.202208764.

47. F. Ding, W. Xu, G. L. Graff, et al., "Dendrite-Free Lithium Deposition via Self-Healing Electrostatic Shield Mechanism," *Journal of the American Chemical Society* 135 (2013): 4450–4456, https://doi.org/10.1021/ja312241y.

48. H. Tang, N. Hu, L. Ma, et al., "Interfacial Dual-Modulation via Cationic Electrostatic Shielding and Anionic Preferential Adsorption toward Planar and Reversible Zinc Electrodeposition," *Advanced Functional Materials* 34 (2024): 2402484, https://doi.org/10.1002/adfm.202402484.

49. P. Wang, S. Liang, C. Chen, et al., "Spontaneous Construction of Nucleophilic Carbonyl-Containing Interphase toward Ultrastable Zinc-Metal Anodes," *Advanced Materials* 34 (2022): 2202733, https://doi.org/10.1002/adma.202202733.

50. M. Zhou, Y. Chen, G. Fang, and S. Liang, "Electrolyte/Electrode Interfacial Electrochemical Behaviors and Optimization Strategies in Aqueous Zinc-Ion Batteries," *Energy Storage Materials* 45 (2022): 618–646, https://doi.org/10.1016/j.ensm.2021.12.011.

51. Z. Shi, S. Chen, M. Zan, et al., "Surfactant-Mediated Mesoscopic Confinement and Selective Interfacial Shielding for Highly Stable Zinc Anode," *Energy & Environmental Science* 19 (2026): 1385–1392, https://doi.org/10.1039/d5ee06338h.

52. S. Zhang, K. Lolupiman, D. Zhang, et al., "Dual-Region Synergistic Modulation and (101) Facet Engineering for Highly Reversible Zinc Anodes," *Advanced Powder Materials* 5 (2026): 100359, https://doi.org/10.1016/j.apmate.2025.100359.

53. B. Lee, H. R. Seo, H. R. Lee, et al., "Critical Role of pH Evolution of Electrolyte in the Reaction Mechanism for Rechargeable Zinc Batteries," *ChemSusChem* 9 (2016): 2948–2956, https://doi.org/10.1002/cssc.201600702.

54. W. Zhang, Y. Dai, R. Chen, et al., "Highly Reversible Zinc Metal Anode in a Dilute Aqueous Electrolyte Enabled by a pH Buffer Additive," *Angewandte Chemie International Edition* 62 (2022): 202212695, https://doi.org/10.1002/anie.202212695.

55. H. Liu, Q. Ye, D. Lei, et al., "Molecular Brush: an Ion-Redistributor to Homogenize Fast Zn^{2+} Flux and Deposition for Calendar-Life Zn Batteries," *Energy & Environmental Science* 16 (2023): 1610–1619, https://doi.org/10.1039/d2ee03952d.

56. C. Huang, F. Huang, X. Zhao, et al., "Rational Design of Sulfonamide-Based Additive Enables Stable Solid Electrolyte Interphase for Reversible Zn Metal Anode," *Advanced Functional Materials* 33 (2022): 2210197, https://doi.org/10.1002/adfm.202210197.

57. H. Liu, J.-G. Wang, W. Hua, et al., "Building Ohmic Contact Interfaces toward Ultrastable Zn Metal Anodes," *Advanced Science* 8 (2021): 2102612, https://doi.org/10.1002/advs.202102612.

58. Y. Yang, C. Liu, Z. Lv, et al., "Synergistic Manipulation of Zn^{2+} Ion Flux and Desolvation Effect Enabled by Anodic Growth of a 3D ZnF_2 Matrix for Long-Lifespan and Dendrite-Free Zn Metal Anodes," *Advanced Materials* 33 (2021): 2007388, https://doi.org/10.1002/adma.202007388.

59. Z. Zhang, Y. Zhang, M. Ye, et al., "Lithium Bis(oxalate)Borate Additive for Self-Repairing Zincophilic Solid Electrolyte Interphases towards Ultrahigh-Rate and Ultra-Stable Zinc Anodes," *Angewandte Chemie International Edition* 62 (2023): 202311032, https://doi.org/10.1002/anie.202311032.

60. G. M. Hobold, K.-H. Kim, and B. M. Gallant, "Beneficial vs. inhibiting Passivation by the Native Lithium Solid Electrolyte Interphase Revealed by Electrochemical Li+ Exchange," *Energy & Environmental Science* 16 (2023): 2247–2261, https://doi.org/10.1039/d2ee04203g.

61. Q. Zhao, Y. Deng, N. W. Utomo, et al., "On the Crystallography and Reversibility of Lithium Electrodeposits at Ultrahigh Capacity," *Nature Communications* 12 (2021): 6034, https://doi.org/10.1038/s41467-021-26143-9.

62. H. Lu, X. Zhang, M. Luo, et al., "Amino Acid-Induced Interface Charge Engineering Enables Highly Reversible Zn Anode," *Advanced Functional Materials* 31 (2021): 2103514, https://doi.org/10.1002/adfm.202103514.

63. J. Cao, X. Rao, S. Qian, et al., "Dynamic Zn^{2+} -Coordinating Oxygen Sites and Electric Field Modulation in Boron-Integrated Cellulose Nanofiber Separators for Stable Zinc-Ion Batteries," *Advanced Energy Materials* 15 (2025), https://doi.org/10.1002/aenm.202503368.

64. Y. Jin, J. Qin, J. Cao, et al., "Fused-Ring Topology Orchestrates Crystallographic Control and Polyiodide Sequestration for Ultra-Durable Zinc–Iodine Batteries," *Energy & Environmental Science* 19 (2026): 1266–1281, https://doi.org/10.1039/d5ee07366a.

65. Z. Liu, S. Chen, Z. Shi, et al., "Multivalent Dipole Interactions-Driven Supramolecular Polymer Layer Enables Highly Stable Zn Anode under Harsh Conditions," *Advanced Energy Materials* 15 (2025): 2502010, https://doi.org/10.1002/aenm.202502010.

66. P. Li, Z. Zhao, Y. Fei, H. Zhang, and G. Li, "$LiNO_3$ -Based Electrolyte with Fast Kinetics for Lithium Metal Batteries under Practical Conditions," *Advanced Energy Materials* 15 (2025): 2500882, https://doi.org/10.1002/aenm.202500882.

67. L. Wu, J. Zhang, Y. Li, et al., "Hydrofluorocarbon Electrolytes for Energy-Dense and Low-Temperature Batteries," *Nature* 651 (2026): 383–389, https://doi.org/10.1038/s41586-026-10210-6.

68. J. Dong, H. Peng, J. Wang, et al., "Molecular Deciphering of Hydrophobic, Zinc-Philic and Robust Amino-Functionalized Polysilane for Dendrite-Free Zn Anode," *Energy Storage Materials* 54 (2022): 875–884, https://doi.org/10.1016/j.ensm.2022.11.026.

69. Y. Liao, H.-C. Chen, C. Yang, et al., "Unveiling Performance Evolution Mechanisms of MnO_2 Polymorphs for Durable Aqueous Zinc-Ion Batteries," *Energy Storage Materials* 44 (2021): 508–516, https://doi.org/10.1016/j.ensm.2021.10.039.

70. Y. Kim, Y. Park, M. Kim, J. Lee, K. J. Kim, and J. W. Choi, "Corrosion as the Origin of Limited Lifetime of Vanadium Oxide-based Aqueous Zinc Ion Batteries," *Nature Communications* 13 (2022): 2371, https://doi.org/10.1038/s41467-022-29987-x.

71. H. Sun, Y. Huyan, N. Li, et al., "A Seamless Metal–Organic Framework Interphase with Boosted Zn^{2+} Flux and Deposition Kinetics for Long-Living Rechargeable Zn Batteries," *Nano Letters* 23 (2023): 1726–1734, https://doi.org/10.1021/acs.nanolett.2c04410.

72. C. Yan, F. He, L. Feng, et al., "Interfacial Molecule Engineering Builds Tri-Functional Bilayer Silane Films with Hydrophobic Ion Channels for Highly Stable Zn Metal Anode," *Advanced Functional Materials* 35 (2025): 2503493, https://doi.org/10.1002/adfm.202503493.

Supporting Information

Additional supporting information can be found online in the Supporting Information section.

Supporting File: adfm74981-sup-0001-SuppMat.docx.

Supporting Video: adfm74981-sup-0002-VideoS1.mp4.